



Allosteric activation of VCP, an AAA unfoldase, by small molecule mimicry

Natalie H. Jones^{a,b} , Qiwen Liu^a, Linas Urnavicius^a, Noa E. Dahan^{a,c} , Lauren E. Vostal^{a,b}, and Tarun M. Kapoor^{a,1}

Edited by Michelle R. Arkin, University of California San Francisco, San Francisco, CA; received October 2, 2023; accepted April 17, 2024

by Editorial Board Member Yifan Cheng

The loss of function of AAA (ATPases associated with diverse cellular activities) mechanoenzymes has been linked to diseases, and small molecules that activate these proteins can be powerful tools to probe mechanisms and test therapeutic hypotheses. Unlike chemical inhibitors that can bind a single conformational state to block enzyme function, activator binding must be permissive to different conformational states needed for mechanobiology. However, we do not know how AAA proteins can be activated by small molecules. Here, we focus on valosin-containing protein (VCP)/p97, an AAA unfoldase whose loss of function has been linked to protein aggregation-based disorders, to identify druggable sites for chemical activators. We identified VCP ATPase Activator 1 (VAA1), a compound that dose-dependently stimulates VCP ATPase activity up to ~threefold. Our cryo-EM studies resulted in structures (ranging from ~2.9 to 3.7 Å-resolution) of VCP in apo and ADP-bound states and revealed that VAA1 binds an allosteric pocket near the C-terminus in both states. Engineered mutations in the VAA1-binding site confer resistance to VAA1, and furthermore, modulate VCP activity. Mutation of a phenylalanine residue in the VCP C-terminal tail that can occupy the VAA1 binding site also stimulates ATPase activity, suggesting that VAA1 acts by mimicking this interaction. Together, our findings uncover a druggable allosteric site and a mechanism of enzyme regulation that can be tuned through small molecule mimicry.

mechanoenzyme | AAA protein | activator | small molecule | cryo-EM

Proteins from the AAA superfamily of mechanoenzymes carry out essential functions across cell biology, including DNA replication, cytoskeleton remodeling, and membrane repair (1). AAA proteins are often hexameric and use energy released during ATP hydrolysis in their AAA domains to carry out mechanical work on different macromolecular substrates (2). The AAA mechanoenzyme VCP extracts or unfolds proteins associated with organelles or in complex cellular assemblies and its activity is central to numerous cellular processes, including endoplasmic reticulum-associated degradation (ERAD), autophagy, chromosome-associated degradation, and ribosome-associated quality control (3–5). Consistent with these important roles, VCP dysfunction is linked to several degenerative diseases, such as multisystem proteinopathy (MSP), amyotrophic lateral sclerosis (ALS), and vacuolar tauopathy, which shares characteristics with Alzheimer's disease (6, 7). To probe the function of VCP in these processes, chemical tools to acutely perturb VCP function have been useful (8). However, the structural basis of VCP activation is not known.

Structural data from crystallography and cryo-EM studies have provided key information about the domain organization of VCP and its overall mechanism (9–11). VCP assemblies as a hexamer, and each VCP monomer consists of a globular N-terminal domain, two AAA domains (D1/D2), linker regions, and a likely disordered C-terminal tail (Fig. 1*A*) (12). Multiple lines of evidence indicate long-range allostery in VCP between its domains. For example, numerous protein cofactors regulate VCP function and direct it to specific, often ubiquitinated, substrates (5, 13). Distinct cofactors can bind the N-terminal domain and/or the C-terminal tail and can have inhibitory or stimulatory effects on VCP (14–16). Furthermore, small chemical changes such as point mutations and posttranslational modifications across VCP's domains can increase or decrease its activity (14, 17–19). Finally, well-characterized chemical inhibitors of VCP have been reported and there are extensive structural data revealing how these compounds bind the enzyme D2 active site or an allosteric site (at the interface between the D1 and D2 domains) (8). However, the identification of allosteric binding sites for small molecule activators remains challenging.

Mutations in VCP have been linked to neurodegenerative diseases (6, 7). Interestingly, distinct disease-associated mutations can result in reduced, no change to, or elevated basal VCP activity, but loss-of-function models better represent disease phenotypes (7, 18, 20).

Significance

Dysfunction of valosin-containing protein (VCP/p97), a mechanoenzyme from the AAA superfamily that hydrolyzes ATP and uses the released energy to extract or unfold substrate proteins, has been linked to protein aggregation-based disorders. However, how VCP, or any AAA mechanoenzyme, can be activated by a drug-like compound is not known. Here, we report cryo-EM structures of VCP in two states in complex with VAA1, a compound we identified that dose-dependently stimulates VCP's ATP hydrolysis activity. Increased VCP ATPase activity also results from mutating a C-terminal tail phenylalanine that can occupy the VAA1-binding site, suggesting that VAA1 may disrupt this interaction. Our study reveals a druggable allosteric site and a mechanism of mechanoenzyme regulation.

Author contributions: N.H.J. and T.M.K. designed research; N.H.J., Q.L., L.U., N.E.D., and L.E.V. performed research; N.H.J., Q.L., and N.E.D. contributed new reagents/analytic tools; N.H.J., Q.L., L.U., and N.E.D. analyzed data; and N.H.J. and T.M.K. wrote the paper.

Competing interest statement: T.M.K. is a co-founder of and has an ownership interest in RADD Pharmaceuticals, Inc.

This article is a PNAS Direct Submission. M.R.A. is a guest editor invited by the Editorial Board.

Copyright © 2024 the Author(s). Published by PNAS. This article is distributed under Creative Commons Attribution-NonCommercial-NoDerivatives License 4.0 (CC BY-NC-ND).

¹To whom correspondence may be addressed. Email: kapoor@rockefeller.edu.

This article contains supporting information online at <https://www.pnas.org/lookup/suppl/doi:10.1073/pnas.2316892121/-DCSupplemental>.

Published June 4, 2024.

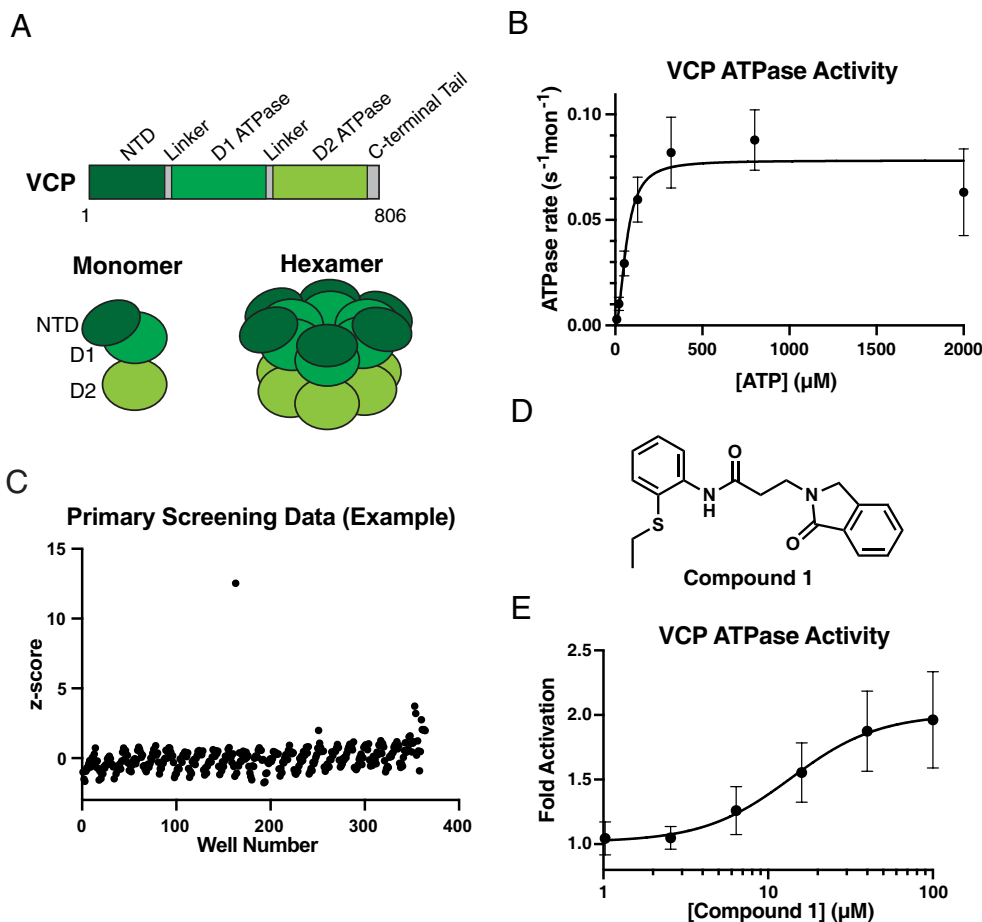


Fig. 1. Screening for small-molecule activators of VCP's ATPase activity. (A) Schematics showing full-length VCP as a domain diagram (light gray box, not to scale, with the first and last residues and domains indicated), a monomer, and a hexamer. Colors indicate different domains. NTD = N-terminal domain. (B) ATP concentration dependence of the steady-state activity of VCP, analyzed using a Malachite Green assay. Rates were fit to the Michaelis-Menten equation for cooperative enzymes (mean \pm SD, $N = 6$ independent experiments) (mon = monomer). (C) Calculated z-scores for compounds from a single screening plate tested in the ADPGlo assay. (D) Structure of Compound 1. (E) Concentration-dependent activation of the ATPase activity of VCP by Compound 1 (100 μ M ATP, 1 h endpoint ADPGlo assay). Graph shows fold activation relative to DMSO control fit to a sigmoidal dose-response equation (mean \pm SD, $N = 9$ independent experiments) (maximum fold activation of 2.2 ± 0.5 , EC_{50} of 15 ± 4 μ M).

Chemical tools and a better understanding of VCP allostery would help test hypotheses for treating these diseases, and small molecule activators of VCP have been recently reported (21–23). Currently, it is unclear if these compounds adhere to typical standards for physicochemical properties of drug-like molecules. For example, the activator SMER28 is a minimally substituted quinazoline, with a low molecular weight (~ 260 Da), and may have multiple cellular targets (22). Currently, we lack the essential structural and mechanistic information needed to design drug-like activators of VCP.

In this manuscript, we identified a compound, which we named VCP ATPase Activator 1 (VAA1), that dose-dependently stimulates the ATPase activity of VCP, saturating at \sim threefold activation. Next, cryo-electron microscopy (cryo-EM) revealed that VAA1 binds in an allosteric pocket near the VCP C terminus in both the apo and ADP-bound states. Finally, we engineered point mutations in the VAA1-binding pocket and show that they confer resistance to VAA1 and stimulate or suppress VCP ATPase activity. Together, our data identify a regulatory site in VCP that can be targeted by small-molecule activators.

Results

Identification of a Chemical Activator of VCP ATPase Activity.

To identify a small molecule activator of VCP, we focused on the full-length protein (Fig. 1A). VCP was purified using a published

procedure with modifications (19), with four steps in total, which generated a recombinant untagged construct at $\sim 93\%$ purity (SI Appendix, Fig. S1 A and B) (Materials and Methods). We characterized this construct using two assays. First, we carried out mass photometry experiments, which revealed a homogeneous species with a molecular weight distributed around 533 ± 6 kDa, consistent with a hexamer in solution (predicted hexamer molecular weight: 536 kDa) (SI Appendix, Fig. S1C). Second, we measured kinetic parameters for ATP hydrolysis ($k_{cat} = 0.084 \pm 0.006$ s^{-1} , $K_{1/2} = 71 \pm 9$ μ M, mean \pm SD, $N = 6$) (Fig. 1B and SI Appendix, Table S1) that are similar to previous reports (14, 17).

For the primary screen for VCP activators, we established an ATPase assay with optimized conditions that would result in ~ 10 to 15% substrate conversion at ATP concentrations near the $K_{1/2}$ (100 μ M). Under these conditions (Z' : 0.85), screening $\sim 35,000$ compounds (20 μ M) resulted in a hit rate of 0.23% (cutoffs: z-score > 2 , > 1.2 -fold activation) (Fig. 1C, example data from a single plate). Hit compounds were retested in three assays: 1) using screening conditions, 2) against assay reagents in a counterscreen, and 3) across a range of doses. Validated dose-responsive hits represented five chemotypes. The most potent hit ("Compound 1") contains an isoindoline heterocycle and an aniline with a thioether substitution (Fig. 1D). Compound 1 was resynthesized (SI Appendix, Supplementary Note) and found to stimulate VCP activity in two different ATPase assays (maximum fold activation of 2.2 ± 0.5 , EC_{50} of 15 ± 4 μ M, mean \pm SD, $N = 9$, 100 μ M ATP, ADPGlo assay;

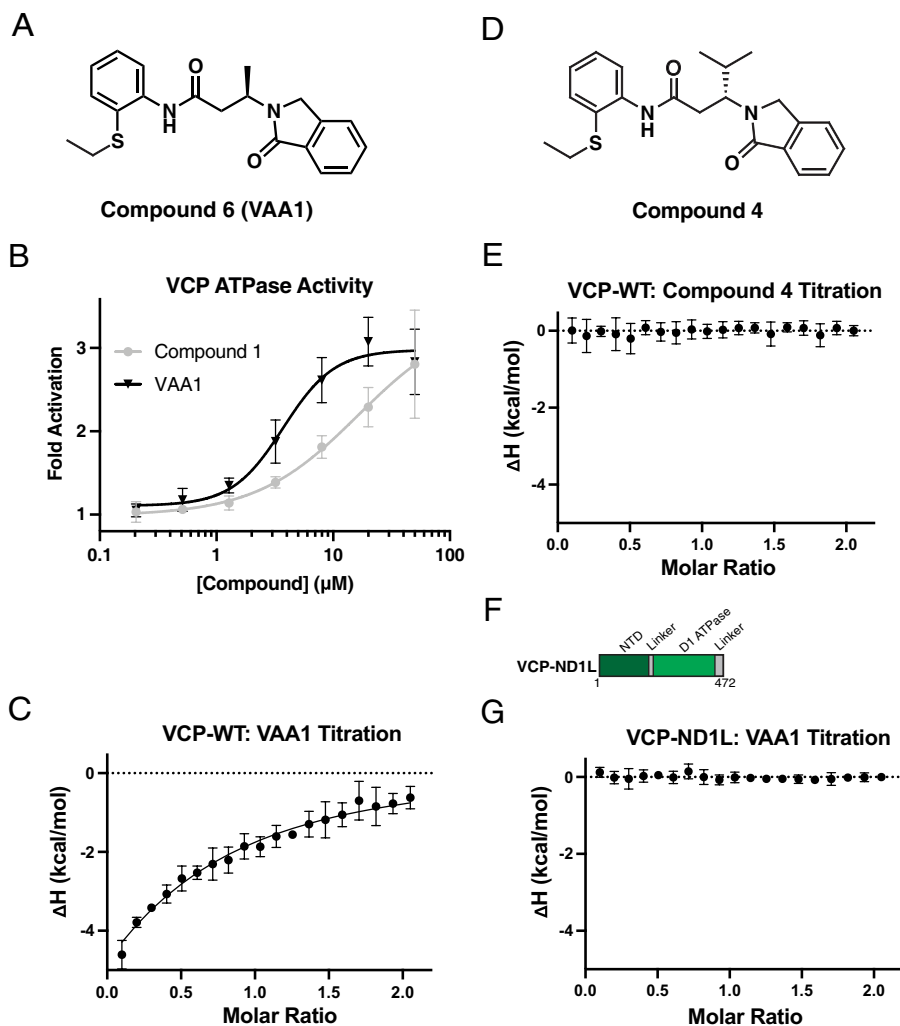


Fig. 2. Analyzing direct binding of small-molecule activators to VCP. (A) Structure of Compound 6 (VAA1). (B) Concentration-dependent activation of the ATPase activity of VCP by Compound 1 and VAA1 (100 μ M ATP, 1 h endpoint assay, ADPGlo). Graph shows fold activation relative to DMSO control fit to a sigmoidal dose-response equation (mean \pm SD, $N = 3$ independent experiments for Compound 1, $N = 5$ independent experiments for VAA1). (C) Integrated data points and fitted binding curve used to determine K_D value from isothermal titration calorimetry (ITC)-based analysis of VCP in the presence of VAA1 (mean \pm SD, $N = 3$ independent experiments). (D) Structure of Compound 4. (E) Integrated data points from ITC-based analysis of VCP in the presence of Compound 4 (mean \pm SD, $N = 3$ independent experiments). (F) Schematic showing the VCP-ND1L construct as a domain diagram (light gray box, not to scale, with the first and last residues and domains identified) (color-coded as in Fig. 1A). (G) Integrated data points from ITC-based analysis of VCP-ND1L in the presence of VAA1 (mean \pm SD, $N = 3$ independent experiments).

similar results were obtained using a colorimetric assay) (Fig. 1E and SI Appendix, Fig. S1D). At a higher ATP concentration (1 mM), dose-dependent activation of VCP by Compound 1 was also observed (maximum fold activation of 2.7 ± 0.6 , EC_{50} of $23 \pm 7 \mu$ M, mean \pm SD, $N = 3$, ADPGlo assay) (SI Appendix, Fig. S1E). Finally, we tested different enzyme concentrations and observed reduced levels of activation at higher enzyme concentrations but did not observe a substantial effect of enzyme concentration on the EC_{50} of activation, consistent with a mechanism of activation that is not aggregation-mediated (SI Appendix, Fig. S1F). Together, these data suggest that Compound 1 can stimulate the ATPase activity of VCP.

Analyzing Chemical Activator Binding to VCP. We next synthesized and tested analogs of Compound 1 (Compounds 2–6, SI Appendix, Table S2, syntheses described in SI Appendix, Supplementary Note). Modification of the thioether substitution in Compound 1 reduces VCP activation. Modifications to the linker region of the compound resulted in both improvements and losses in potency. For example, Compounds 4 and 5 represent an enantiopair, and the observed differences in their potencies suggest

that VCP activation results from direct and specific interactions between the chemical scaffold and the enzyme. For additional studies, we focused on Compound 6 (hereafter, VCP ATPase Activator 1/VAA1), which has more desirable properties ($cLogP$ of 4.1 for Compound 5 versus 3.4 for VAA1). VAA1 shows a ~threefold increase in potency over Compound 1 (maximum fold activation of 3.0 ± 0.3 , EC_{50} of $4.1 \pm 1.1 \mu$ M, mean \pm SD, $N = 5$, 100 μ M ATP) (Fig. 2A and B). Consistent with an allosteric activation mechanism, VAA1 treatment increases the k_{cat} of VCP, but does not substantially affect its $K_{1/2}$ for ATP (DMSO control: $k_{cat} = 0.10 \pm 0.03 s^{-1}$, $K_{1/2} = 79 \pm 8 \mu$ M; 20 μ M VAA1: $k_{cat} = 0.19 \pm 0.04 s^{-1}$, $K_{1/2} = 76 \pm 10 \mu$ M; mean \pm SD, $N = 3$) (SI Appendix, Fig. S2A).

To test whether VAA1 makes direct interactions with VCP, we used isothermal titration calorimetry (ITC). The observed binding isotherm could be fit to a K_D of $27 \pm 4 \mu$ M (mean \pm SD, $N = 3$) (Fig. 2C). Importantly, similar experiments with the inactive analog Compound 4 did not indicate any binding to VCP (Fig. 2D and E). We next examined whether the N-terminal and D1 domains, which can bind protein cofactors that activate VCP (11, 14, 24–26), can be activated and bound by VAA1. We

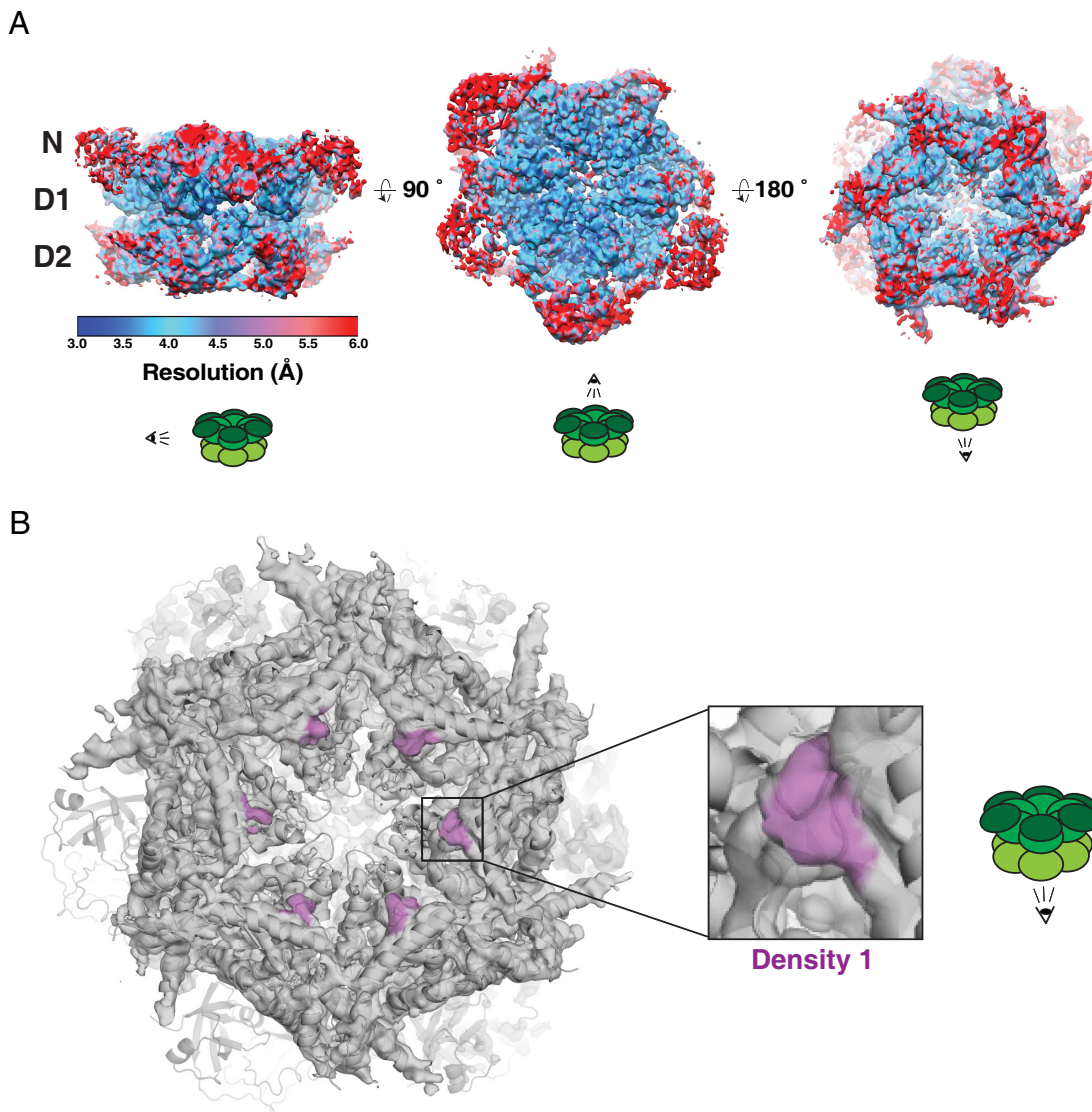


Fig. 3. Cryo-EM analysis of VCP in the presence of VAA1. (A) Three views of the overall VCP density analyzed by ResMap (28), showing a resolution distribution from 3.0 to 6.0 Å. (B) Molecular model of VCP (cartoon representation) in the density map (Left, semitransparent surface). The Inset shows extra density (magenta) that could not be assigned to VCP or bound nucleotides.

purified a truncated construct with the VCP N-terminal and D1 domains (aa 1 to 472, hereafter VCP-ND1L) (Fig. 2F and SI Appendix, Fig. S2B) (Materials and Methods) and found its ATPase activity to be lower than that of the full-length protein, consistent with the role of the D2 domain as a key source of hydrolysis activity ($k_{\text{cat}} = 0.032 \pm 0.01 \text{ s}^{-1}$, $K_{1/2} = 49 \pm 7 \text{ } \mu\text{M}$, mean \pm SD, $N = 3$) (SI Appendix, Fig. S2C and Table S1) (27). Interestingly, VAA1 did not stimulate the ATPase activity of VCP-ND1L (up to 50 μM , ADPGlo assay) (SI Appendix, Fig. S2D). Additionally, we did not observe binding of VAA1 to VCP-ND1L in ITC experiments under similar conditions to those used for full-length VCP (Fig. 2G). Together, these data suggest that VAA1 stimulates VCP ATPase activity through direct interactions, likely involving the D2 domain.

Structural Analysis of VAA1 Binding VCP. To examine how VAA1 binds VCP, we employed single-particle cryo-EM. We incubated VCP with VAA1 (200 μM), prepared grids, and observed homogenous, monodisperse particles in our micrographs (SI Appendix, Fig. S2E and Table S3 and Materials and Methods). Autopicked particles were cleaned by multiple rounds of 2D classification yielding class averages that resemble the VCP

hexamer (SI Appendix, Figs. S2F and S3A and Materials and Methods). 3D classification to balance views and 3D refinement without symmetry of the cleaned particles from these classes resulted in an overall map of the VCP hexamer resolved to $\sim 3.9 \text{ } \text{\AA}$ (Fig. 3A and SI Appendix, Figs. S3A and S4A). The core resolved to $\sim 3.5 \text{ } \text{\AA}$ to $4.0 \text{ } \text{\AA}$, revealing side chain detail, and the periphery resolved to $\geq 5.5 \text{ } \text{\AA}$, revealing secondary structure detail (Fig. 3A).

We used rigid body docking to fit the N-terminal, D1, and D2 domains of a published ADP-bound VCP structure (PDB: 5FTL) (10) and C-terminal tail residues 763 to 775 resolved in a peptide substrate-bound VCP structure (PDB: 7LN6) (11) into our map. The D1 and D2 domains occupy the core, and the N-terminal domains and C-terminal tails, which are more dynamic (10, 11), are positioned at the periphery (Fig. 3A and B). Close inspection of our map revealed a density in the D2 domain in each monomer that could not be assigned to the VCP backbone or sidechains or bound nucleotides (hereafter, “Density 1”) (Fig. 3B). Density 1 is localized between adjacent D2 nucleotide binding sites and the central pore, in a region that is well resolved (Fig. 3A and B). Together, our findings with VCP-ND1L (Fig. 2G) and our structural data suggest that Density 1 could represent VAA1 (Fig. 3B).

VAA1 Binds VCP in Apo and ADP-Bound States of the D2 Domain.

To better characterize the binding site containing Density 1, we carried out additional processing steps, focusing on the D2 domain, as signal subtraction from raw images followed by focused 3D refinement has proven useful for resolution improvements in other structures of large complexes (29–32). We additionally applied C6 symmetry to obtain a map that resolved to ~ 3.5 Å (*SI Appendix, Fig. S4 B and C*), and we could observe detailed interactions between Density 1 and nearby amino acid side chains. Only minor adjustments (real space sphere refinement within Coot and real space refinement within Phenix; see *Materials and Methods*) to the docked VCP coordinates were required (*SI Appendix, Fig. S5A*). As nucleotide was not observed bound to the D2 domain, we hereafter refer to this dataset as “VCP-VAA1-apo”.

To fit a model for VAA1 in Density 1, we used computational modeling (Maestro Macromodel, Schrodinger LLC), which generated a bent conformation of the compound, with the isoindoline and aniline proximal to each other. This shape of VAA1 matches Density 1; the density is stronger for the aromatic rings than for the smaller amide linker, which is likely due to the current resolution (Fig. 4A and *SI Appendix, Fig. S5A*). In comparisons of our VAA1-bound structure to a published VCP structure in the apo state, at the current resolution, we did not observe major conformational changes in the motifs that comprise the VAA1 binding site (*SI Appendix, Fig. S5B*) (33). To address the weaker density for the amide linker, we focused on a small fraction (<5%) of particles corresponding to 2D classes that appeared to represent a VCP dodecamer in our cryo-EM data, a dimer of hexamers that has been observed in other cryo-EM studies of VCP (*SI Appendix, Figs. S2F and S3A*) (33–36). Signal subtraction and focused refinement with D6 symmetry on the D2 domains resulted in a map resolved to ~ 2.9 Å (“VCP-VAA1-apo-dodec”) (*SI Appendix, Figs. S3A and S4 D and E*). Gratifyingly, we observed a density that agrees with Density 1 from the VCP hexamer map and additionally shows continuous density between the isoindoline and aniline (Fig. 4B and *SI Appendix, Fig. S5C*), matching our VAA1 binding model. The narrower side of Density 1 accommodates the thioether substitution on the aniline and orients into a cleft proximal to Arg625 (Fig. 4C). In this binding mode, the isoindoline is positioned near Met757 and Phe758 in the C-terminal helix (Fig. 4D).

We next examined whether VAA1 can bind to VCP in other nucleotide states in addition to the apo state. We incubated VCP with VAA1 (50 μ M) and subsequently added ATP (100 μ M) before preparing grids (*SI Appendix, Fig. S3B and Table S3*, “VCP-VAA1-ADP” dataset). Following data collection, 2D classification and 3D refinement (*SI Appendix, Fig. S3B*) resulted in a map of the VCP hexamer D2 domains resolved to ~ 3.7 Å (Fig. 4E and *SI Appendix, Figs. S4 F and G*). Individual domains of published VCP structures (PDB 5FTL for the D2 domains with C-terminal tail residues 763–774 from PDB 7LN6) (10, 11) were rigid body docked and refined into the map (Fig. 4E). VAA1 occupancy and orientation relative to nearby side chains is consistent between VCP-VAA1-apo and VCP-VAA1-ADP (Fig. 4F and *SI Appendix, Fig. S5D*). We observed density corresponding to ADP, the hydrolyzed product of the added ATP, in the D2 active site, confirming that a different nucleotide state than apo is compatible with VAA1 binding (Fig. 4G). VAA1 binding did not result in substantial changes to the C-terminal helix or nearby loops compared to a published structure with ADP bound, at the resolution of these structures (*SI Appendix, Fig. S5E*) (10). We observed different states of pore loop II, which is proximal to the VAA1 binding site, in our two structures, with a more stable pore loop in VCP-VAA1-ADP than VCP-VAA1-apo (*SI Appendix, Fig. S5F*). Furthermore, the

N-domain adopted a variety of conformations in our conditions (both with and without the addition of ATP) as indicated by 3D classification results in our cryo-EM processing (*SI Appendix, Fig. S5G*). Together, our structural data indicate that VAA1 binds a site near the VCP C-terminus in both apo and ADP-bound states of the D2 domain.

The VAA1 Binding Site Allosterically Regulates VCP Activity. To probe the role of the VAA1 binding site and test our compound binding model, we designed mutations in the C-terminal helix: 1) Tyr755-His, as a conservative mutation, and 2) Lys754-Asn, which is the amino acid at the equivalent position in the related AAA protein PEX1, a mutagenesis approach we have employed for other AAA proteins (37–39) (*Materials and Methods*). We generated full-length recombinant VCP-K754N and VCP-Y755H and characterized these constructs using ATPase assays (*SI Appendix, Fig. S6 A and B and Table S1*). The mutant constructs show $K_{1/2}$ values similar to that of the WT protein, but, notably, different k_{cat} values than that of the WT protein ($\sim 40\%$ lower for VCP-K754N; \sim twofold higher for VCP-Y755H) (VCP-K754N: $K_{1/2} = 93 \pm 7$ μ M, $k_{\text{cat}} = 0.051 \pm 0.02$ s^{-1} ; VCP-Y755H: $K_{1/2} = 83 \pm 5$ μ M, $k_{\text{cat}} = 0.17 \pm 0.02$ s^{-1} ; mean \pm SD, $N = 3$) (Fig. 5 A and B and *SI Appendix, Fig. S6B and Table S1*). Importantly, VAA1 did not stimulate the ATPase activities of VCP-K754N or VCP-Y755H (Fig. 5C). We additionally assessed binding for VCP-Y755H using ITC and observed no measurable binding of VAA1 to VCP-Y755H (*SI Appendix, Fig. S6C*).

To examine whether VCP constructs with disease-associated mutations are activated by our compounds, we focused on Asp592-Asn, a mutation near the VAA1 binding site that has been linked to ALS (40). We generated a recombinant construct of full-length VCP with the D592N mutation (*Materials and Methods*) and characterized its ATP hydrolysis activity (*SI Appendix, Fig. S6 A and B*). The D592N mutation reduces both the $K_{1/2}$ for ATP and the k_{cat} by $\sim 40\%$ ($K_{1/2} = 42 \pm 9$ μ M, $k_{\text{cat}} = 0.049 \pm 0.009$ s^{-1} , mean \pm SD, $N = 3$) (Fig. 5 A and B and *SI Appendix, Fig. S6B, Table S1*). However, VAA1 treatment stimulates the activity of VCP-D592N, with an EC_{50} comparable to the WT protein (\sim twofold activation, EC_{50} of 3.6 ± 0.9 μ M, mean \pm SD, $N = 4$, 1 mM ATP) (Fig. 5D). Our data suggest that resistance-conferring mutations in the VAA1 binding site can modulate ATP turnover by VCP, and while a disease mutation proximal to the binding site reduces enzymatic activity, it does not substantially affect VAA1-mediated activation.

We next analyzed the VAA1 binding site in available structures of the VCP hexamer. In our VAA1-bound structures, the C-terminal tail is positioned between helices $\alpha 6$ and $\alpha 8$ of the neighboring D2 domain (Fig. 5E). In contrast, in previously solved structures of VCP in an ATP γ S-bound D2 state, the C-terminal tail orients toward the neighboring D2 nucleotide binding site (10, 36, 41) (Fig. 5E). In this conformation, the side chain of Phe-768, a residue in the tail, occupies the VAA1 binding pocket (Fig. 5E). To examine the role of interactions made by Phe-768, we designed and generated a full-length recombinant VCP-F768A construct and tested it using ATPase and ITC assays (*SI Appendix, Fig. S6 A and B*). The F768A mutation increases the $K_{1/2}$ for ATP by $\sim 70\%$, and, notably, the k_{cat} by ~ 2.1 -fold ($K_{1/2} = 120 \pm 6$ μ M, $k_{\text{cat}} = 0.19 \pm 0.02$ s^{-1} , mean \pm SD, $N = 3$) (Fig. 5 A and B and *SI Appendix, Fig. S6B and Table S1*). VAA1 did not substantially stimulate the ATPase activity of VCP-F768A (Fig. 5F). To test whether, as for VCP-Y755H, this loss of stimulation was correlated with loss of binding, we used ITC. Interestingly, we observed a binding isotherm for the VAA1/VCP-F768A interaction that could be fit to a K_D of 26 ± 10 μ M (mean \pm SD, $N = 3$), similar to that measured for VAA1/VCP-WT (Fig. 5G).

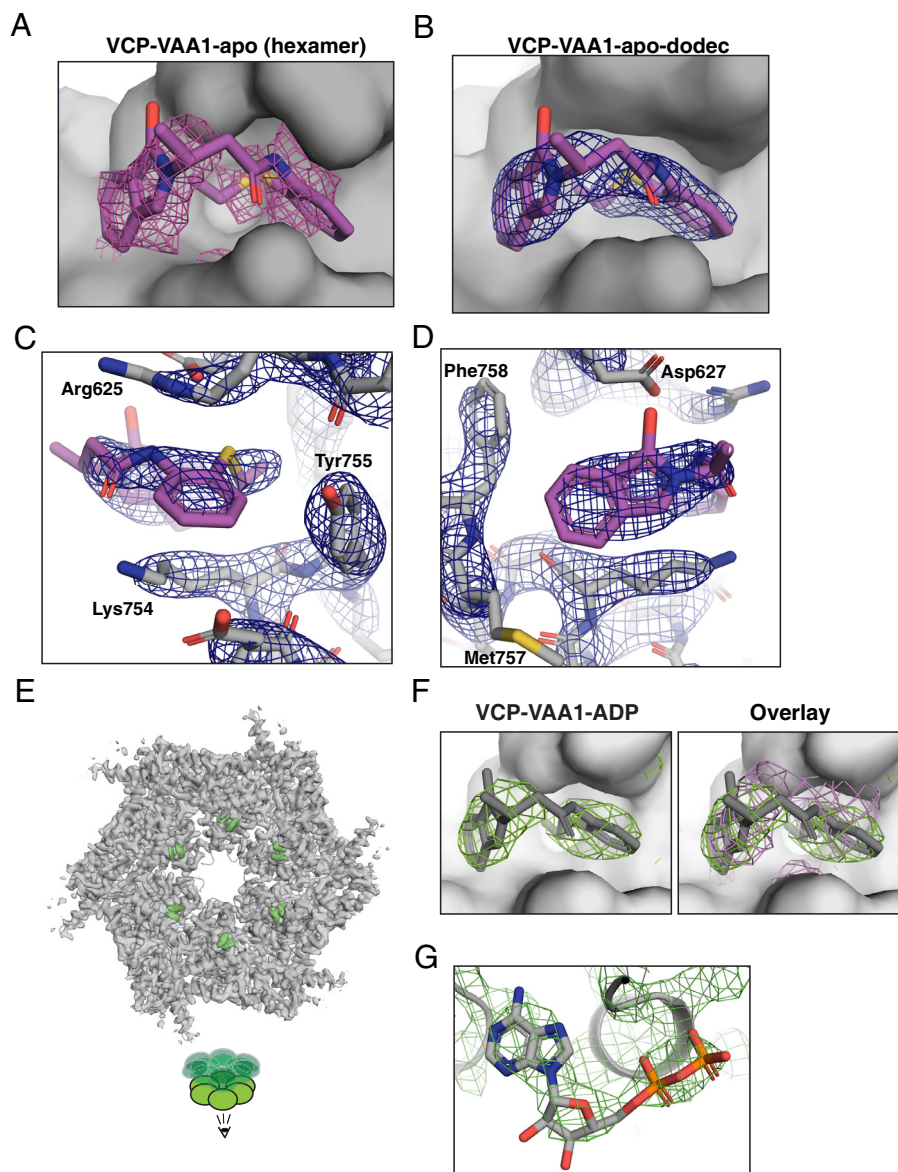


Fig. 4. Structural analysis of VAA1 binding VCP in distinct states. (A) Model of VAA1 in the proposed binding site in VCP-VAA1-apo (VAA1, magenta, stick representation; VCP model, gray, surface representation; VCP hexamer cryo-EM density, magenta, mesh). (B) Model of VAA1 in the proposed binding site in VCP-VAA1-apo-dodec (VAA1, magenta, stick representation; VCP, gray, surface representation; VCP dodecamer cryo-EM density, blue, mesh). (C) View showing the fit of the VAA1 thioether aniline (magenta, stick representation) as well as nearby residues (gray, stick representation) within the VCP-VAA1-apo-dodec density map (mesh). (D) View showing the fit of the VAA1 isoindoline (magenta, stick representation) as well as nearby residues (gray, stick representation) within the VCP-VAA1-apo-dodec density map (mesh). (E) Molecular model of the VCP D2 domains (gray cartoon representation) within the VCP-VAA1-ADP density map (gray surface with VAA1 density highlighted in green). (F) Panels showing the VAA1 binding site, comparing maps for datasets with and without the addition of ATP (VAA1, gray, stick representation; VCP model, gray, surface representation; VCP-VAA1-ADP density, green, mesh; VCP-VAA1-apo density, magenta, mesh). (G) Panel showing the D2 nucleotide binding site for VCP-VAA1-ADP (ADP, stick representation; VCP, gray, cartoon representation; density, green, mesh).

These data suggest that the F768A mutation stimulates VCP activity and confers resistance to VAA1-mediated activation, yet does not substantially affect VAA1 binding to VCP.

Discussion

Here, we report an allosteric site in VCP that can be bound by a small-molecule activator. We identified VAA1, a small molecule that stimulates VCP ATPase activity, and carried out cryo-EM studies of VCP in complex with VAA1 in ADP-bound and apo states of the D2 active site. Engineered mutations in the VAA1-binding pocket can confer resistance to VAA1 and result in either increases or decreases in VCP ATP turnover, suggesting the sensitivity of the enzyme to modulation of this allosteric site. Further, mutating a

C-terminal tail residue results in an increase in VCP ATP turnover, consistent with VAA1 stimulating activity by mimicking the intra-molecular interactions between this residue and the VCP D2 domain.

VCP's C-terminal tail is a conformationally dynamic motif that lacks stable secondary structure but is nonetheless functionally relevant. The C-terminal tail has been proposed to contain at least three phosphorylation sites (Thr-761, Ser-784, and Tyr-805) (19, 42–45). Additionally, a subset of VCP cofactors, including UBXD1, PLAA, and PNGase, have been proposed to bind the C-terminal tail (16, 46–49). In our VAA1-bound structures, the C-terminal tail is positioned between helices $\alpha 6$ and $\alpha 8$ of the neighboring D2 domain, whereas in structures of VCP in an ATP γ S-bound D2 state, the C-terminal tail orients toward the neighboring D2 nucleotide binding site (10, 36, 41) (Fig. 5E).

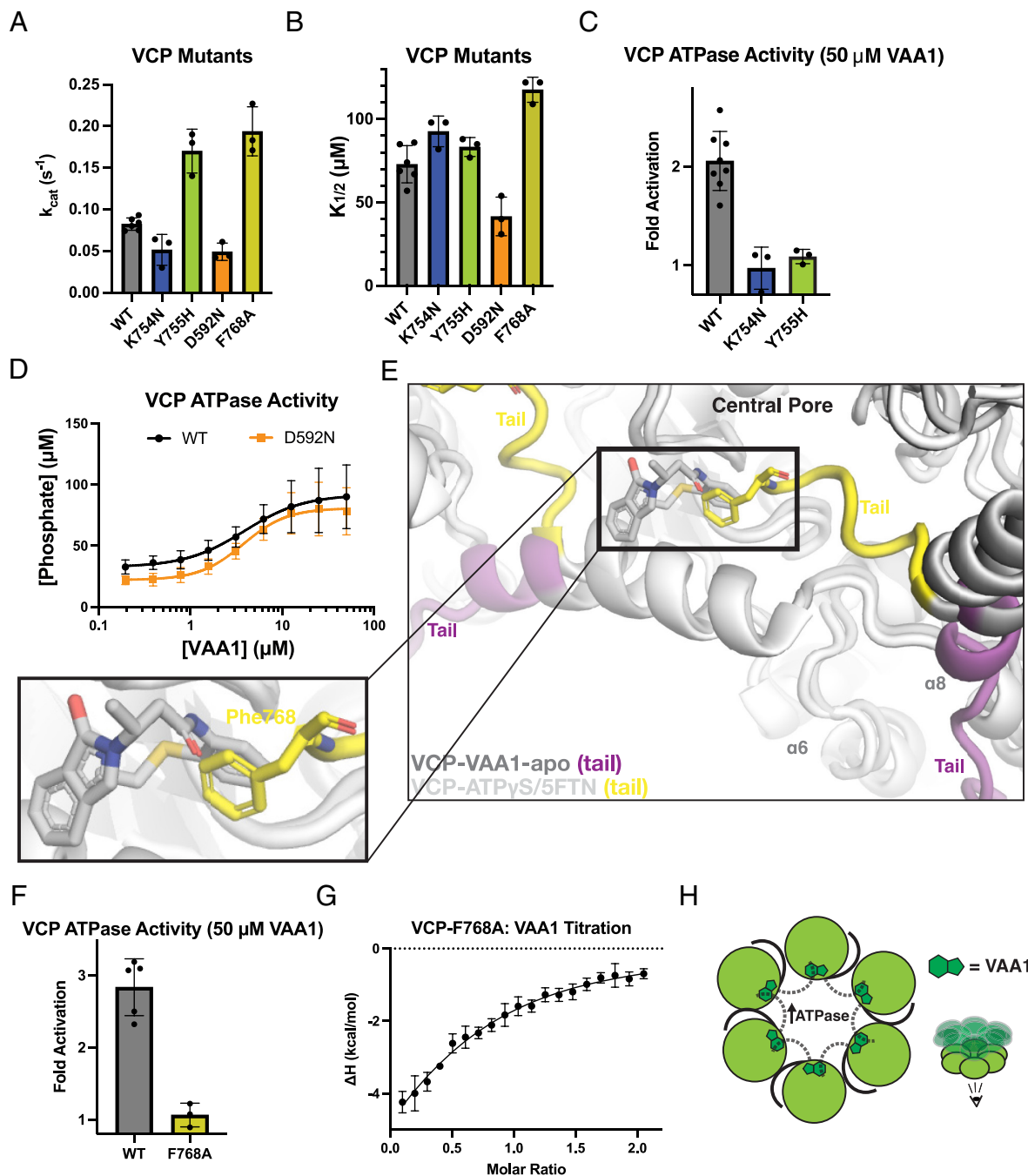


Fig. 5. Characterization of the VAA1 binding site and a model for allosteric activation of VCP's ATPase activity. (A and B) Effect of the K754N, Y755H, D592N, and F768A mutations on VCP enzymatic activity. Graphs show values for the turnover number (k_{cat} , A) and ATP concentration required for half-maximal velocity ($K_{1/2}$, B) of VCP-WT, -K754N, -Y755H, -D592N, and -F768A constructs, analyzed by measuring the steady-state ATPase rate across a range of ATP concentrations using a Malachite Green assay (mean \pm SD, $N = 6$ independent experiments for WT; $N = 3$ independent experiments for mutants). (C) Fold change in ATPase activity of VCP (WT and K754N and Y755H mutants) in the presence of VAA1 (50 μM ATP, 1 h endpoint assay) (mean \pm SD, $N = 7$ independent experiments for VCP-WT; mean \pm SD, $N = 3$ independent experiments for VCP-K754N and VCP-Y755H). (D) VCP ATPase activity (WT and D592N mutant) in the presence of VAA1 (1 mM ATP, 1 h endpoint assay) (mean \pm SD, $N = 4$ independent experiments). (E) Alignment of VCP-VAA1-apo (cartoon representation, gray, with C-terminal tails in magenta and VAA1 in stick representation) and VCP-ATP γ S (PDB: 5FTN) (cartoon representation, white, with C-terminal tails in yellow and Phe-768 in stick representation). *Inset* focuses on VAA1. (F) Fold change in ATPase activity of VCP (WT and F768A mutant) in the presence of VAA1 (100 μM ATP, 1 h endpoint assay) (mean \pm SD, $N = 5$ independent experiments for VCP-WT, data from Fig. 2B; mean \pm SD, $N = 3$ independent experiments for VCP-F768A). (G) Integrated data points and fitted binding curve used to determine K_D value from ITC-based analysis of VCP-F768A in the presence of VAA1 (mean \pm SD, $N = 3$ independent experiments). (H) Schematic for VAA1 binding to VCP in a site that can be occupied by the C-terminal tail. VAA1 accelerates ATP turnover by VCP by displacing the tail, which is autoinhibitory. Dashed line indicates potential occupancy of the tail at the VAA1 binding site. Sixfold symmetry is assumed.

In the ATP γ S-bound state, the Phe-768 side chain occupies the VAA1-binding pocket and Arg-766 coordinates the ATP γ S γ -phosphate (Fig. 5E and *SI Appendix*, Fig. S6D). Our results suggest that mutation of Phe-768 to alanine stimulates ATPase activity and allows for binding of VAA1 that does not result in

further enzyme activation (Fig. 5). VAA1 binding may structurally mimic the interactions made by Phe-768 with the D2 domain, and, further, the displacement of the C-terminal tail from the VAA1 binding site may enhance enzymatic activity (Fig. 5H). Our data suggest that the C-terminal tail binding in

the VAA1 binding site represents a partially autoinhibited state of VCP. Consistent with the role of this site for regulation of VCP activity, we observed changes in turnover number (k_{cat}) with the introduction of the K754N and Y755H mutations, which may also alter interactions made by Phe-768 in the binding site (Fig. 5A and *SI Appendix, Table S1*). Together, these data suggest that VCP's C-terminal tail and the motifs with which it interacts in VCP form an important regulatory site that can be targeted by small-molecule activators.

Accumulation of toxic protein aggregates is a common feature of degenerative diseases (50). VCP disassembles aggregated proteins in vitro and in cells, suggesting its activation as a means of removing disease aggregates (7). Further to this rationale for activating wild-type VCP, mutations in VCP have been linked to degenerative diseases by multiple lines of evidence, including cell biological studies, mouse models, and patient sequencing data (6, 7). Loss of VCP ATPase activity can result from mutations such as the D395G mutation associated with vacuolar tauopathy and the ALS-associated D592N mutation characterized herein (7). Other mutations result in no change to or an increase in VCP's ATPase activity, but the activity level does not correlate with disease severity, and, importantly, in some cases disease phenotypes are better represented by loss-of-function models (18, 20). In addition, these mutations may cause an altered equilibrium between conformational states of the N-terminal domain in cells, consistent with measured changes in VCP's affinity for certain cofactors (e.g., the Ufd1/Npl4 complex and UBXD1) (18, 51, 52). Testing differential binding of cofactors in the presence of chemical activators may help dissect this further. By modulating VCP activity, experiments with both chemical inhibitors and activators of VCP can also help examine its potential to clear disease aggregates in general. Finally, chemical activators may stimulate activity by a different mechanism than ATPase-activating MSP-associated mutations (which are localized in the N/D1 domains) and thus help deconvolute their paradoxical effects in vitro versus in cellulo. At this stage, the micromolar potency of VAA1 may limit its measurable on-target activity in cells. However, with our structural data and mechanistic hypothesis for activation, structure-based drug design campaigns should lead to more potent activators.

Protein cofactors known to stimulate VCP ATPase activity bind near the N terminus (11, 14, 15, 25), but the dispersed surface contacts involved in protein–protein interactions may not be readily recapitulated by small molecule binders. The VAA1 binding site is distinct from this N-terminal regulatory site and suggests a mechanism of activation that may be compatible with multiple VCP interacting partners. We note that the primary structural elements that comprise the VAA1 binding site, namely, the loop containing Arg-625/Asp-627 and the C-terminal helix, are conserved in a subset of AAA proteins, and could function as a regulatory site for these mechanoenzymes. Interestingly, it is possible that the VAA1 binding pocket could serve as a binding site for cellular metabolites that regulate AAA proteins. The structures of VCP in complex with VAA1 open the door to rational design of activators targeting an allosteric regulatory site in this AAA protein whose function is central to cellular proteostasis.

Materials and Methods

Plasmids. Plasmid for expressing wild-type *Homo sapiens* VCP was obtained from T.-F. Chou (Caltech). Plasmids for VCP mutants were generated by site-directed mutagenesis (including VCP-ND1L, which was generated by mutating Gln-473 to a stop codon).

Expression and Purification of VCP Constructs. The VCP constructs were expressed in *Escherichia coli* Rosetta (DE3) pLysS cells (Merck, cat. No. 70954) grown in Miller's LB medium (LMM, Formedium, cat. No. LMM105). Culture growth at 37 °C was monitored by measuring absorbance at 600 nm (A_{600}), and protein expression was induced at $A_{600} \approx 0.7$ with 0.5 mM IPTG (GoldBio). The culture was grown at 18 °C for ~15 h, pelleted, and resuspended in lysis buffer [50 mM K. HEPES pH 7.5, 400 mM KCl, 20 mM imidazole, 5% glycerol, 5 mM β -mercaptoethanol, 200 μ M MgATP, 1 mM *p*-phenylmethylsulfonyl fluoride, cOmplete EDTA-free protease inhibitor cocktail (Roche)]. All subsequent purification steps were performed at 4 °C. Cells were lysed using an EmulsiFlex C5 homogenizer (Avestin, ~6 cycles at 10,000 to 15,000 psi homogenization pressure). The lysate was clarified by centrifugation at 45,000 rpm for 30 min using a Type 70 Ti rotor in a Beckman Coulter Optima LE-80 K ultracentrifuge.

The clarified lysate was loaded onto Ni-NTA resin and incubated for 1 to 2 h. The resin was washed with ~200 mL of wash buffer (50 mM K. HEPES pH 7.5, 400 mM KCl, 20 mM imidazole, 5% glycerol, 5 mM β -mercaptoethanol, 200 μ M MgATP) and eluted with elution buffer (50 mM K. HEPES pH 7.5, 400 mM KCl, 300 mM imidazole, 5% glycerol, 5 mM β -mercaptoethanol, 100 μ M MgATP). The eluate was treated with tobacco etch virus (TEV) protease (~2 mg) and dialyzed in dialysis buffer (50 mM K. HEPES pH 7.5, 100 mM KCl, 20 mM imidazole, 1 mM MgCl_2 , 5% glycerol, 5 mM β -mercaptoethanol, 100 μ M MgATP) overnight. Protein was passed three times over Ni-NTA resin pre-equilibrated with reverse Ni buffer (25 mM K. HEPES pH 8, 100 mM KCl, 20 mM imidazole, 1 mM MgCl_2 , 5% glycerol, 5 mM β -mercaptoethanol) or incubated 1 h then eluted. Protein was loaded onto a Q column (GE Healthcare) pre-equilibrated with low salt buffer (25 mM K. HEPES pH 8, 100 mM KCl, 1 mM MgCl_2 , 5% glycerol, 2 mM DTT) and eluted in a 0 to 100% gradient of high salt buffer (50 mM K. HEPES pH 8, 500 mM KCl, 1 mM MgCl_2 , 5% glycerol, 2 mM DTT) over 40 mL. Fractions containing VCP were concentrated using an Amicon Ultra 50 K concentrator to 1 to 2 mL, centrifuged to remove precipitate, and loaded into a Superdex 200 16/600 column (GE Healthcare) equilibrated with gel filtration buffer (50 mM K. HEPES pH 7.5, 200 to 250 mM KCl, 1 to 2 mM MgCl_2 , 5% glycerol, 1 mM reducing agent (DTT or TCEP)). The fractions containing purified VCP were pooled, concentrated using an Amicon Ultra 50 K concentrator, and frozen in liquid nitrogen and stored at -80 °C.

Mass Photometry. Data were collected using a OneMP mass photometer (Refeyn) calibrated with bovine serum albumin (ThermoFisher, cat. No. 23210), beta amylase (Sigma Aldrich, cat. No. A8781-1VL), and thyroglobulin (Sigma Aldrich, cat. No. T9145-1VL). Focus was adjusted using filtered (0.22 μ m) phosphate-buffered saline (PBS), then a 400 nM solution of VCP in filtered PBS with 2% DMSO was added directly, diluting it fourfold. Movies were acquired for 6,000 frames (60 s) using AcquireMP software (version 2.4.0) and default settings. Raw data were converted to frequency distributions using DiscoverMP software (10 kDa bin size) and Gaussian fits were applied to determine the average mass for each peak.

Analysis of ATPase Activity. The ATPase activity of VCP was examined using Malachite Green and ADPGlo assays. For Malachite Green assays to determine kinetic parameters, incubation of VCP with ATP proceeded for different time points before simultaneous addition of reagent to read out phosphate production as absorbance at 620 nm using a Synergy NEO microplate reader. The rates from control reactions without VCP were subtracted from the corresponding reactions with VCP at the same [ATP]. VCP was assayed at 100 to 200 nM in 50 mM K. HEPES pH 7.5, 25 mM KCl, 2.5 mM MgCl_2 , 2.5 mM GSH, 0.01% Triton-X-100, 0.1 mg/mL BSA. Analyses of activators were carried out in the same conditions, with a 5 min preincubation of VCP with compound before addition of ATP, and, for dose-response analyses, a single 60 min time point of enzymatic activity. The final DMSO concentration was 0.5%. ADPGlo assays to test activators were carried out under the same ATPase reaction conditions as Malachite Green assays to test activators, except using 10 to 100 nM VCP. After reagent incubations, the generation of ADP was measured as luminescence using a Synergy NEO microplate reader.

In line with our previous work on AAA proteins, we analyzed the kinetic parameters of VCP using a modified Michaelis–Menten equation, which includes a Hill coefficient (37–39):

$$V = \text{ATPase rate} = \frac{(V_{\max} x^h)}{(K_{1/2}^h + x^h)},$$

where V_{\max} is the maximum ATPase rate, h is the Hill coefficient, x is ATP concentration, and $K_{1/2}$ is the concentration of ATP required for half-maximal enzyme rate. The $K_{1/2}$ term distinguishes this constant from the standard Michaelis-Menten constant K_m . Catalytic turnover number (k_{cat}) was calculated by dividing V_{\max} by the concentration of VCP in the assay.

For the compound EC_{50} determination, for each experiment the fold-change in enzyme activity in the presence of compound compared to control was plotted against compound concentrations, and the data were fit using a sigmoidal dose-response curve equation:

$$Y = Y_{\min} + \left(\frac{(Y_{\max} - Y_{\min})}{\left(1 + 10^{(\log EC_{50} - x)h}\right)} \right)$$

Small-Molecule Activator Screening Protocol. The Z' of the ADPGlo assay with conditions used for screening was 0.85. The screening campaign was performed against a ~35,000-compound library in a 384-well format. After a 5 min preincubation of 25 nM VCP with 20 μ M compound, ATP was added to 100 μ M and the reaction was allowed to proceed for 60 min (~10 to 15% ATP consumption in controls) before addition of ADPGlo reagent (40 min incubation) and Kinase Detection Reagent (40 min incubation). The hit rate using a $2 \times$ SD (~20% activation) cutoff was ~0.23%. Primary hits that repeated with the same experimental setup, but did not result in increased luminescence in the absence of VCP, were tested for dose responsiveness. Dose-responsive hits with favorable physicochemical and structural characteristics were repurchased from the supplier for retesting, and Compound **1** was selected as the highest potency compound.

Isothermal Titration Calorimetry. ITC measurements were performed using a MicroCal auto-iTC200 calorimeter (MicroCal). Purified VCP constructs were diluted to 30 μ M in 50 mM K. HEPES pH 7.5, 25 mM KCl, 2.5 mM $MgCl_2$, 1 mM TCEP, 0.01% Triton-X-100, and DMSO was added to 0.6%. A separate buffer solution was prepared to match the final concentrations of components accounting for the contribution of the buffer the VCP was stored in. Final assay buffer concentrations were 50 mM K. HEPES pH 7.5, 30 to 64 mM KCl, 2.5 mM $MgCl_2$, 0 to 0.1 mM DTT, 1 mM TCEP, 0.1 to 1.1% glycerol, 0.008 to 0.01% Triton-X-100. DMSO solutions of compounds were diluted in the assay buffer to 30 μ M (0.6% DMSO, final concentration) and titrated into the diluted VCP in the ITC chamber (25 $^{\circ}$ C, stirring at 750 rpm). Titrations were carried out with 19 injections of 2 μ L, with a duration of 4 s per injection and spacing of 150 s. Independent titrations of the same compound solutions into buffer (with 0.6% DMSO, without VCP) were carried out and subtracted from the data for the titrations into VCP. The data were analyzed using MicroCal PEAQ-ITC software and plotted using Prism (version 9.2, GraphPad Software). Dissociation constants from each titration of VAA1 into full-length VCP-WT were obtained using a single-site equilibrium-binding model, carried out in the MicroCal PEAQ-ITC software.

Cryo-EM Sample Preparation. Full-length VCP-WT was buffer exchanged into 50 mM K. HEPES pH 7.5, 25 mM KCl, 2.5 mM $MgCl_2$, 2.5 mM GSH using an Amicon Ultra 100 K concentrator and concentrated to ~1 mg/mL. For the dataset without nucleotide (VCP-VAA1-apo), VAA1 (200 μ M, 0.5% DMSO, final concentrations) was added and incubated at room temperature 5 min and then, fluorinated octyl maltoside (FOM) detergent was added (0.01% (w/v) final concentration). The sample was applied to Graphene Oxide on Quantifoil R2/2 300-square-mesh copper grids. The samples were incubated on grids on a FEI Vitrobot IV for 30 s and blotted for 3.5 to 4 s at 100% humidity and 25 $^{\circ}$ C (force: 0, wait time: 0 s), then plunged into liquid ethane.

For the dataset with the addition of nucleotide (VCP-VAA1-ADP), VAA1 (50 μ M, 0.5% DMSO, final concentrations) was added, and the sample was incubated at room temperature for 5 min. MgATP (100 μ M, final concentration) was subsequently added to the VCP/VAA1 sample and incubated at room temperature for 5 min and then, fluorinated octyl maltoside (FOM) detergent was added (0.01% w/v final concentration). The sample was applied to freshly glow-discharged (30 s) Quantifoil R2/2 300-square-mesh copper grids and blotted for 3.5 to 4 s at 100% humidity and 25 $^{\circ}$ C (force: 0, wait time: 0 s) on a FEI Vitrobot IV, then plunged into liquid ethane.

Cryo-EM Data Collection. Micrographs were recorded using automated data collection (SerialEM or Legion) (53, 54) on a FEI Titan Krios with a Gatan K2 or K3 camera in super-resolution mode. Collection settings (acceleration voltage, camera, CS corrector, energy filter, exposure time, frame number, pixel size, dose) are listed in *SI Appendix, Table S3*.

Cryo-EM Data Processing. Correction of interframe movement for each pixel and dose-weighting was performed using MotionCor2 or Relion's own implementation (55–57). CTF parameters were estimated using CTFFIND4 (58). Further processing was carried out using Relion v.3.1 or v.4.0 (56, 57). For VCP-VAA1-apo, a small set of particles was manually picked and subjected to 2D classification to generate references for automated particle picking. Autopicked particles were cleaned with multiple rounds of 2D classification and subsequently selected hexamer and dodecamer classes. Cleaned hexamer particles were subjected to 3D classification to select a subset of higher quality particles with well-balanced orientations. These particles were subjected to global 3D refinement without symmetry to yield an overall VCP reconstruction. To improve density near the proposed VAA1 binding site, we generated a mask for the D2 domains and performed signal subtraction to remove N-terminal domain and D1 domain signal from raw particle images. Subtracted particles were subjected to local 3D refinement with C6 symmetry. Other datasets were similarly processed with minor modifications (*SI Appendix, Fig. S3*).

Cryo-EM Model Building. A VCP model (5FTL) was segmented into N-terminal, D1, and D2 domains for each chain, and coordinates for residues 763 to 775 of the C-terminal tail were segmented from another VCP model (7LN6). Each segment was rigid body fitted in Chimera (59) and Coot ("jiggle fit" function) (60). These docked domains were joined to generate the overall VCP hexamer model. For each symmetric structure masked on the D2 domains (VCP-VAA1-apo C6 hexamer, VCP-VAA1-apo D6 dodecamer, VCP-VAA1-ADP C6 hexamer), real space sphere refinement in Coot with torsion, planar peptide, trans peptide, and Ramachandran restraints enforced was used to adjust side chains for a single chain. These refined coordinates were replicated and refit into the density for the total of 6 (hexamer) or 12 (dodecamer) chains. Models were further refined using phenix.real_space_refine (61), and problem areas were fixed manually in COOT. Refinement statistics for each structure are summarized in *SI Appendix, Table S4*.

Data, Materials, and Software Availability. Density maps and associated coordinates data have been deposited in PDB and EMDB [VCP-VAA1-apo (C6 hexamer): [8VKU](#), [EMD-43329](#) (62, 63); VCP-VAA1-apo (D6 dodecamer): [8VLS](#), [EMD-43343](#) (64, 65); VCP-VAA1-ADP (C6 hexamer): [8VOV](#), [EMD-43392](#) (66, 67)].

ACKNOWLEDGMENTS. We thank T.-F. Chou for providing the *H. sapiens* VCP plasmid. T.M.K. is grateful to the NIH (GM130234) for funding. N.H.J. was supported in part by the NSF Graduate Research Fellowship Program (1946429). L.E.V. was supported in part by the NIH T32 GM115327 and GM136640 Chemistry-Biology Interface Training Grant to the Tri-Institutional PhD Program in Chemical Biology. This work was supported in part by The Rockefeller University Robertson Therapeutic Development Fund and The Rockefeller University Kellen Women's Entrepreneurship Fund. We are grateful to the Fisher Drug Discovery Resource Center at The Rockefeller University for assistance with the high-throughput screen and instrument use. We thank M. Ebrahim, J. Sotiris, and H. Ng, the Evelyn Gruss Lipper Cryo-Electron Microscopy Resource Center for Cryo-EM support. Some of this work was also performed at the Simons Electron Microscopy Center (SEMC) at the New York Structural Biology Center, with major support from the Simons Foundation (SF349247). We are also grateful to A. Xue for technical assistance with postprocessing of Cryo-EM data.

Author affiliations: ^aLaboratory of Chemistry and Cell Biology, The Rockefeller University, New York, NY 10065; ^bTri-Institutional PhD Program in Chemical Biology, New York, NY 10065; and ^cThe David Rockefeller Graduate Program in Bioscience, The Rockefeller University, New York, NY 10065

1. C. Puchades, C. R. Sandate, G. C. Lander, The molecular principles governing the activity and functional diversity of AAA+ proteins. *Nat. Rev. Mol. Cell Biol.* **21**, 43–58 (2020).
2. T. V. Seraphim, W. A. Houry, AAA+ proteins. *Curr. Biol.* **30**, R251–R257 (2020).

3. N. Bodnar, T. Rapoport, Toward an understanding of the Cdc48/p97 ATPase. *F1000Res.* **6**, 1318 (2017).
4. Y. Ye, W. K. Tang, T. Zhang, D. Xia, A. Mighty, "Protein Extractor" of the cell: Structure and function of the p97/CDC48 ATPase. *Front. Mol. Biosci.* **4**, 39 (2017).

5. J. van den Boom, H. Meyer, VCP/p97-mediated unfolding as a principle in protein homeostasis and signaling. *Mol. Cell* **69**, 182–194 (2018).
6. H. Meyer, C. C. Wehl, The VCP/p97 system at a glance: Connecting cellular function to disease pathogenesis. *J. Cell Sci.* **127**, 3877–3883 (2014).
7. N. F. Darwich *et al.*, Autosomal dominant VCP hypomorph mutation impairs disaggregation of PHF-tau. *Science* **370**, eaay8826 (2020).
8. D. M. Huryn, D. J. P. Kornfilt, P. Wipf, p97: An emerging target for cancer, neurodegenerative diseases, and viral infections. *J. Med. Chem.* **63**, 1892–1907 (2020).
9. J. M. Davies, A. T. Brunger, W. I. Weis, Improved structures of full-length p97, an AAA ATPase: Implications for mechanisms of nucleotide-dependent conformational change. *Structure* **16**, 715–726 (2008).
10. S. Banerjee *et al.*, 2.3 Å resolution cryo-EM structure of human p97 and mechanism of allosteric inhibition. *Science* **351**, 871–875 (2016).
11. M. Pan *et al.*, Mechanistic insight into substrate processing and allosteric inhibition of human p97. *Nat. Struct. Mol. Biol.* **28**, 614–625 (2021).
12. D. Xia, W. K. Tang, Y. Ye, Structure and function of the AAA+ ATPase p97/Cdc48p. *Gene* **583**, 64–77 (2016).
13. D. Barthelme, R. T. Sauer, Origin and functional evolution of the Cdc48/p97/VCP AAA+ protein unfolding and remodeling machine. *J. Mol. Biol.* **428**, 1861–1869 (2016).
14. X. Zhang *et al.*, Altered cofactor regulation with disease-associated p97/VCP mutations. *Proc. Natl. Acad. Sci. U.S.A.* **112**, E1705–E1714 (2015).
15. E. E. Blythe, K. C. Olson, V. Chau, R. J. Deshaies, Ubiquitin- and ATP-dependent unfoldase activity of P97/VCP•NPLC4•UFD1L is enhanced by a mutation that causes multisystem proteinopathy. *Proc. Natl. Acad. Sci. U.S.A.* **114**, E4380–E4388 (2017).
16. J. R. Braxton *et al.*, The p97/VCP adaptor UBXD1 drives AAA+ remodeling and ring opening through multi-domain tethered interactions. *Nat. Struct. Mol. Biol.* **30**, 2009–2019 (2023).
17. Y. Wei, J. I. Toth, G. A. Blanco, A. A. Bobkov, M. D. Petroski, Adapted ATPase domain communication overcomes the cytotoxicity of p97 inhibitors. *J. Biol. Chem.* **293**, 20169–20180 (2018).
18. E. E. Blythe, S. N. Gates, R. J. Deshaies, A. Martin, Multisystem proteinopathy mutations in VCP/p97 increase NPLC4-UFD1L binding and substrate processing. *Structure* **27**, 1820–1829 (2019).
19. B. Wang *et al.*, ULK1 and ULK2 regulate stress granule disassembly through phosphorylation and activation of VCP/p97. *Mol. Cell* **74**, 742–757.e8 (2019).
20. A. Wani *et al.*, Neuronal VCP loss of function recapitulates FTLD-TDP pathology. *Cell Rep.* **36**, 109399 (2021).
21. A. Figuerola-Conchas *et al.*, Small-molecule modulators of the ATPase VCP/p97 affect specific p97 cellular functions. *ACS Chem. Biol.* **15**, 243–253 (2020).
22. L. Wrobel *et al.*, Compounds activating VCP D1 ATPase enhance both autophagic and proteasomal neurotoxic protein clearance. *Nat. Commun.* **13**, 4146 (2022).
23. J. M. Phan *et al.*, Novel VCP activator reverses multisystem proteinopathy nuclear proteostasis defects and enhances TDP-43 aggregate clearance. *bioRxiv* [Preprint] (2023). <https://doi.org/10.1101/2023.03.15.532082> (Accessed 1 April 2023).
24. P. Hänzelmann, H. Schindelin, Characterization of an additional binding surface on the p97 N-terminal domain involved in bipartite cofactor interactions. *Structure* **24**, 140–147 (2016).
25. Y. Xu *et al.*, Active conformation of the p97–p47 unfoldase complex. *Nat. Commun.* **13**, 2640 (2022).
26. J. van den Boom, G. Marini, H. Meyer, H. R. Saibil, Structural basis of ubiquitin-independent PP1 complex disassembly by p97. *EMBO J.* **42**, e113110 (2023).
27. W. K. Tang, D. Xia, Role of the D1–D2 linker of human VCP/p97 in the asymmetry and ATPase activity of the D1-domain. *Sci. Rep.* **6**, 20037 (2016).
28. A. Kucukelbir, F. J. Sigworth, H. D. Tagare, Quantifying the local resolution of cryo-EM density maps. *Nat. Methods* **11**, 63–65 (2014).
29. T. H. D. Nguyen, W. P. Galej, X. Bai, C. Oubridge, Cryo-EM structure of the yeast U4/U6. U5 tri-snRNP at 3.7 Å resolution. *Nature* **530**, 298–302 (2016).
30. F. Zeng *et al.*, Structural basis of co-translational quality control by ArfA and RF2 bound to ribosome. *Nature* **541**, 554–557 (2017).
31. A. Nakanishi, J.-I. Kishikawa, M. Tamakoshi, K. Mitsuoka, K. Yokoyama, Cryo EM structure of intact rotary H⁺-ATPase/synthase from *Thermus thermophilus*. *Nat. Commun.* **9**, 89 (2018).
32. L. Urnăvicius *et al.*, Cryo-EM shows how dynactin recruits two dyneins for faster movement. *Nature* **554**, 202–206 (2018).
33. G. Yu *et al.*, Cryo-electron microscopy structures of VCP/p97 reveal a new mechanism of oligomerization regulation. *iScience* **24**, 103310 (2021).
34. M. R. Hoq *et al.*, Affinity capture of p97 with small-molecule ligand bait reveals a 3.6 Å double-hexamer cryoelectron microscopy structure. *ACS Nano* **15**, 8376–8385 (2021).
35. P. Nandi *et al.*, Structural and functional analysis of disease-linked p97 ATPase mutant complexes. *Int. J. Mol. Sci.* **22**, 8079 (2021).
36. H. Gao *et al.*, Cryo-EM structures of human p97 double hexamer capture potentiated ATPase-competent state. *Cell Discov.* **8**, 19 (2022).
37. T. Cupido, R. Pisa, M. E. Kelley, T. M. Kapoor, Designing a chemical inhibitor for the AAA protein spastin using active site mutations. *Nat. Chem. Biol.* **15**, 444–452 (2019).
38. R. Pisa, T. Cupido, J. B. Steinman, N. H. Jones, T. M. Kapoor, Analyzing resistance to design selective chemical inhibitors for AAA proteins. *Cell Chem. Biol.* **26**, 1263–1273.e5 (2019).
39. T. Cupido, N. H. Jones, M. J. Grasso, R. Pisa, T. M. Kapoor, A chemical genetics approach to examine the functions of AAA proteins. *Nat. Struct. Mol. Biol.* **28**, 388–397 (2021).
40. J. O. Johnson *et al.*, Exome sequencing reveals VCP mutations as a cause of familial ALS. *Neuron* **68**, 857–864 (2010).
41. M. Pan *et al.*, Seesaw conformations of Npl4 in the human p97 complex and the inhibitory mechanism of a disulfiram derivative. *Nat. Commun.* **12**, 121 (2021).
42. M. Egerton, L. E. Samelson, Biochemical characterization of valosin-containing protein, a protein tyrosine kinase substrate in hematopoietic cells. *J. Biol. Chem.* **269**, 11435–11441 (1994).
43. M. Livingstone *et al.*, Valosin-containing protein phosphorylation at Ser784 in response to DNA damage. *Cancer Res.* **65**, 7533–7540 (2005).
44. C. Mori-Konya *et al.*, p97/valosin-containing protein (VCP) is highly modulated by phosphorylation and acetylation. *Genes Cells* **14**, 483–497 (2009).
45. C. Zhu *et al.*, Phospho-Ser784-VCP is required for dna damage response and is associated with poor prognosis of chemotherapy-treated breast cancer. *Cell Rep.* **31**, 107745 (2020).
46. G. Zhao *et al.*, Studies on peptide: N-glycanase-p97 interaction suggest that p97 phosphorylation modulates endoplasmic reticulum-associated degradation. *Proc. Natl. Acad. Sci. U.S.A.* **104**, 8785–8790 (2007).
47. L. Qiu *et al.*, Structure and function of the PLAA/Ufd3-p97/Cdc48 complex. *J. Biol. Chem.* **285**, 365–372 (2010).
48. M. Blueggel, J. van den Boom, H. Meyer, P. Bayer, C. Beuck, Structure of the PUB domain from ubiquitin regulatory X domain protein 1 (UBXD1) and its interaction with the p97 AAA+ ATPase. *Biomolecules* **9**, 876 (2019).
49. M. Blueggel *et al.*, The UB domain in UBXD1 organizes ubiquitin binding at the C-terminus of the VCP/p97 AAA-ATPase. *Nat. Commun.* **14**, 3258 (2023).
50. A. Ciechanover, Y. T. Kwon, Degradation of misfolded proteins in neurodegenerative diseases: Therapeutic targets and strategies. *Exp. Mol. Med.* **47**, e147 (2015).
51. D. Ritz *et al.*, Endolysosomal sorting of ubiquitylated caveolin-1 is regulated by VCP and UBXD1 and impaired by VCP disease mutations. *Nat. Cell Biol.* **13**, 1116–1123 (2011).
52. A. K. Schuetz, L. E. Kay, A dynamic molecular basis for malfunction in disease mutants of p97/VCP. *eLife* **5**, e20143 (2016).
53. D. N. Mastronarde, Automated electron microscope tomography using robust prediction of specimen movements. *J. Struct. Biol.* **152**, 36–51 (2005).
54. C. Suloway *et al.*, Automated molecular microscopy: The new Legimon system. *J. Struct. Biol.* **151**, 41–60 (2005).
55. S. Q. Zheng *et al.*, MotionCor2: Anisotropic correction of beam-induced motion for improved cryo-electron microscopy. *Nat. Methods* **14**, 331–332 (2017).
56. J. Zivanov *et al.*, New tools for automated high-resolution cryo-EM structure determination in RELION-3. *eLife* **7**, e42166 (2018).
57. D. Kimanius, L. Dong, G. Sharov, T. Nakane, S. H. W. Scheres, New tools for automated cryo-EM single-particle analysis in RELION-4.0. *Biochem. J.* **478**, 4169–4185 (2021).
58. A. Rohou, N. Grigorieff, CTFFIND4: Fast and accurate defocus estimation from electron micrographs. *J. Struct. Biol.* **192**, 216–221 (2015).
59. E. F. Pettersen *et al.*, UCSF Chimera—a visualization system for exploratory research and analysis. *J. Comput. Chem.* **25**, 1605–1612 (2004).
60. P. Emsley, B. Lohkamp, W. G. Scott, K. Cowtan, Features and development of Coot. *Acta Crystallogr. D Biol. Crystallogr.* **66**, 486–501 (2010).
61. D. Liebschner *et al.*, Macromolecular structure determination using X-rays, neutrons and electrons: Recent developments in Phenix. *Acta Crystallogr. D Struct. Biol.* **75**, 861–877 (2019).
62. N. H. Jones, L. Urnăvicius, T. M. Kapoor, Structure of VCP in complex with an ATPase activator (D2 domains only, hexameric form). Protein Data Bank. <https://www.rcsb.org/structure/8VKU>. Deposited 9 January 2024.
63. N. H. Jones, L. Urnăvicius, T. M. Kapoor, Structure of VCP in complex with an ATPase activator (D2 domains only, hexameric form). Electron Microscopy Data Bank. <https://www.ebi.ac.uk/emdb/EMD-43329>. Deposited 9 January 2024.
64. N. H. Jones, L. Urnăvicius, T. M. Kapoor, Structure of VCP in complex with an ATPase activator (D2 domains only, dodecameric form). Protein Data Bank. <https://www.rcsb.org/structure/8VL5>. Deposited 12 January 2024.
65. N. H. Jones, L. Urnăvicius, T. M. Kapoor, Structure of VCP in complex with an ATPase activator (D2 domains only, dodecameric form). Electron Microscopy Data Bank. <https://www.ebi.ac.uk/emdb/EMD-43343>. Deposited 12 January 2024.
66. N. H. Jones, L. Urnăvicius, T. M. Kapoor, Structure of VCP in complex with an ATPase activator and ADP (D2 domains only, hexameric form). Protein Data Bank. <https://www.rcsb.org/structure/8VOV>. Deposited 16 January 2024.
67. N. H. Jones, L. Urnăvicius, T. M. Kapoor, Structure of VCP in complex with an ATPase activator and ADP (D2 domains only, hexameric form). Electron Microscopy Data Bank. <https://www.ebi.ac.uk/emdb/EMD-43392>. Deposited 16 January 2024.